SHIELD: A Codebook-Based Methodology for RIS-Based Covert Communications

Alexandros I. Papadopoulos*†, Dimitrios Tyrovolas‡, Alexandros Pitilakis‡, Panagiotis D. Diamantoulakis‡, Antonios Lalas*, Konstantinos Votis*, Nikolaos V. Kantartzis‡, Sotiris Ioannidis§, Christos Liaskos†
*Information Technologies Institute, Centre for Research and Technology Hellas (CERTH), Greece
e-mail: {alexpap, lalas, kvotis}@iti.gr
†Computer Science and Engineering Department, University of Ioannina, Greece, e-mail: {apapadopoulos, cliaskos}@uoi.gr
‡Department of Electrical and Computer Engineering, Aristotle University of Thessaloniki, Greece,
e-mail: {tyrovolas, alexpiti, padiaman, kant}@auth.gr
§Department of Electrical and Computer Engineering, Technical University of Crete, Greece,
e-mail: sotiris@ece.tuc.gr

***Abstract*—Programmable Wireless Environments (PWEs) leverage Reconfigurable Intelligent Surfaces (RISes) to actively shape electromagnetic (EM) propagation, enabling advanced control over wireless channels. Beyond improved performance in B5G/6G networks, this control also introduces new security capabilities. Exploiting this, we propose RF-Fencing: a service that selectively suppresses EM signals toward eavesdroppers while preserving reliable communication for legitimate users, thereby significantly enhancing network covertness. Building on that, in this paper, we introduce SHIELD, the first RF-Fencing algorithm that partitions the PWE into Signal Suppression Areas (SSAs) and Signal Delivery Areas (SDAs) through on-the-fly merging of RIS configurations. Extensive EM analysis confirms SHIELD's effectiveness in preventing wardens from intercepting critical information and achieving covert communications with minimal impact on legitimate users. Moreover, SHIELD can serve also as a jamming-mitigation mechanism and is applicable across various frequency bands and RIS designs.**

***Index Terms*—RIS, RF-Fencing, Covert Communications, Jamming Mitigation, EM-wave analysis.**

I. Introduction

The emergence of 6G networks is transforming wireless systems into multifunctional platforms that support extremely high data rates, integrated sensing and communications, advanced location-based services and autonomous mobility. In addition to these capabilities, 6G must also ensure strong privacy guarantees, particularly in sensitive applications where even the detection of a transmission could compromise confidentiality. In this context, covert communications have emerged as a critical strategy, aiming to ensure that wireless transmissions remain entirely undetectable to unintended recipients, thereby protecting both the content and the existence of the communication itself [1]. To meet this dual demand for high performance and strong privacy, the concept of Programmable Wireless Environments (PWEs) has been introduced, enabling dynamic control over wireless propagation through the integration of reconfigurable components into the environment [2]. Central to this vision are Reconfigurable Intelligent Surfaces (RISes), which offer real-time control over incident electromagnetic (EM) waves, enabling precise control of wireless propagation through functionalities such as beam steering and signal absorption [3], [4]. As a result, RISes are increasingly recognized as key enablers of covert wireless services in 6G, allowing the environment itself to suppress or redirect transmissions in a manner that embeds covertness as an intrinsic network feature.

Driven by the paradigm of PWEs, several works have examined how RIS technology can enhance covert communications by shaping the wireless propagation environment. Specifically, [5] demonstrated that a well-configured RIS can redirect or absorb signals to reduce detectability, while later efforts, such as [6], proposed leveraging multi-user interference in full-duplex setups to mask covert transmissions without artificial jamming. More recently, the authors in [7] introduced a multi-RIS covert framework based on distributed reinforcement learning, showing the potential of coordinated RIS control to improve spatial suppression and covert throughput.

Despite significant progress in RIS-based covertness enhancement, existing approaches heavily depend on computationally intensive techniques such as iterative optimization algorithms, machine-learning methods, or detailed channel state information computations. These approaches introduce substantial computational overhead, limiting their real-time applicability. Moreover, current evaluations primarily involve numerical simulations without sufficient integration of accurate physics-based modeling, restricting their accuracy and practical viability. A promising approach to overcoming these challenges is the codebook-based RIS configuration [8], [9]. Here, RIS functionalities are predetermined and accurately aligned with optimal configurations at the manufacturing phase by integrating physics-informed insights and metaheuristic optimization within simulation tools or prototyped measurement setups [2]. These optimal configurations are systematically stored in a Codebook Database. Consequently, during operational deployment, the RIS efficiently retrieves the relevant configuration from the codebook, drastically reducing runtime computational complexity [10].

Furthermore, recent research highlights the capability of multiplexing simple codebook entries to achieve more complex functionalities. This enables a single RIS unit to con-

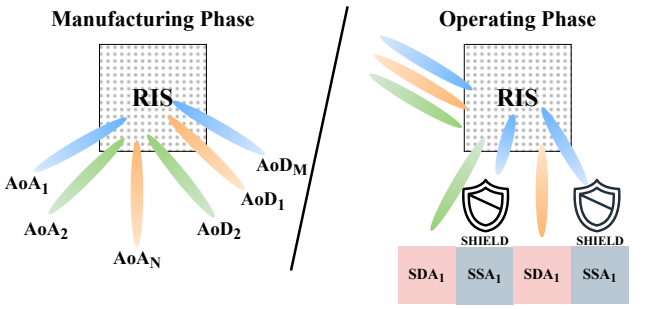

Fig. 1: Manufacturing (left) and Operating (right) phase using RF-Fencing SHIELD algorithm.

currently support multiple spatial tasks with minimal computational overhead, typically in the order of milliseconds [8], [9]. However, to the best of our knowledge, there is currently no framework that simultaneously ensures spatially aware covertness preserving legitimate-user performance, and rigorously validates these outcomes using physics-based simulations within realistic operational environments.

In this paper, we introduce SHIELD, a codebook-based algorithm enabling multi-RIS coordination for spatially-aware covert communication via precomputed RIS configurations. As shown in Fig. 1, SHIELD relies solely on beam-steering codebook entries corresponding to supported angles of arrival (AoA) and departure (AoD), computed offline during manufacturing. During operation, SHIELD selectively nullifies EM signals in designated areas to suppress detection by wardens without impairing legitimate communications. Additionally, if the jammer's location is known, SHIELD can inversely apply the same principle for effective jamming mitigation.

The main contributions of this work are as follows:

- We define *RF-Fencing*, a novel RIS-enabled service that allows PWEs to enforce spatially selective signal suppression, creating EM quiet zones in targeted directions while preserving uninterrupted communication in legitimate areas.
- We develop **SHIELD**, a scalable algorithm that partitions the angular domain into Signal Suppression Areas (SSAs) and Signal Delivery Areas (SDAs), configuring each RIS through multiplexing of configurations drawn from the codebook.
- We evaluate SHIELD through EM-wave analysis across diverse frequency bands, RIS implementations, and spatial layouts, demonstrating its ability to achieve high covert performance while preserving the integrity of legitimate links.

The remainder of this paper is organized as follows: In Section II, we present the RF-fencing service and describe how the RIS is modeled via EM-wave analysis. In Section III, we present the workflow of the proposed SHIELD algorithm. Section IV offers the evaluation of the algorithm for different frequency bands and number of SSAs and SDAs. Finally, Section V concludes the paper.

II. RF-Fencing & RIS Modeling

The realization of spatially-aware covert communication within PWEs depends on the ability to shape wireless propagation with directional precision. To this end, the *RF-Fencing* service is introduced as a novel RIS-enabled functionality that enables the formation of SSAs, where signal emissions are deliberately suppressed or redirected, while ensuring high signal integrity in designated SDAs. This dual capability allows the environment to embed covertness directly into its propagation behavior by controlling the spatial footprint of transmissions. Supporting such behavior in real time requires RIS units to simultaneously deliver multiple EM functionalities, including signal redirection and suppression, without incurring high computational cost during operation. A promising approach is response multiplexing, where complex spatial responses are synthesized by combining simpler, precompiled codebook configurations [8], [9], [11]. These methods eliminate the need for iterative optimization and support fast adaptation across varying network conditions. Nonetheless, accurately assessing their effectiveness requires EM-consistent modeling of RIS behavior, as statistical channel models lack the spatial granularity necessary to evaluate covert performance.

By taking into account the need for accurate yet tractable EM modeling, physical optics emerges as a suitable foundation for capturing the spatial dynamics required by RF-Fencing [12]. Unlike statistical models for the estimation of channel state information that abstract away the underlying wave behavior, this formulation preserves an accurate, physical structure of signal propagation and enables precise characterization of RIS-induced suppression and redirection patterns. In this context, each RIS is modeled as a two-dimensional array composed of $N_{\text{el}} = N_r \times N_c$ reconfigurable unit cells, with all the elements collectively providing the RIS controllable phase profile across its aperture ($\mathbf{\Phi}$). Each element acts as a unitary magnitude and variable phase scattered, where

$$\Phi_{m,n} \in [0, 2\pi], \quad m = 1, \ldots, N_r, \quad n = 1, \ldots, N_c. \tag{1}$$

In more detail, each surface is illuminated by a uniform plane wave characterized by wavelength λ and wavenumber $k_0 = 2\pi/\lambda$, arriving from a far-field direction (θ_i, φ_i), and each unit cell occupies a position on a rectangular grid, with spacing Δ_x and Δ_y along the horizontal and vertical axes, respectively, resulting in the coordinates

$$x_m = \Delta_x(m - m_c), \quad y_n = \Delta_y(n - n_c), \tag{2}$$

where (m_c, n_c) denotes the center of the array and serves as the reference point for evaluating phase differences across the surface. Based on this geometry, the phase of the incident wavefront at each unit cell is given by

$$\psi^{\text{inc}}_{m,n} = k_0 \left[\Delta_x(m - m_c)\cos\varphi_i + \Delta_y(n - n_c)\sin\varphi_i\right]\sin\theta_i. \tag{3}$$

These spatial and phase properties are used to derive the far-field scattered response of the RIS under the Huygens–Fresnel principle (HPF) [12] yielding

$$E(\theta, \varphi) = E_0 \cos^{2\rho}(\theta) \sum_{m=1}^{N_r} \sum_{n=1}^{N_c} \Psi_{m,n}, \tag{4}$$

where E_0 is a normalization constant related to the magnitude of the incident field, measured in V/m and ρ captures the angular selectivity of the scattering pattern, with $\rho = 0$ modeling isotropic behavior. Moreover, the total contribution of each cell is expressed by the $\Psi_{m,n} = e^{j\left[\Phi_{m,n} + \psi_{m,n}^{\text{inc}}\right]}$, includes the phase shift induced by the control element and the phase related to the cell's placement with respect to the incident wavefront. The assumption of a uniform plane wave simplifies the analysis with a controllable limitation of the generality. In face, the HFP formulation can handle also arbitrary incident wavefronts, such as diverging spherical wavefronts from near-field point sources. In these scenarios, the scalar E_0 in Eq. (4) should be simply moved inside the double sum/integral and replaced with a complex, cell-specific field E_0, capturing both phase and magnitude variations across the RIS aperture. Finally, to assess the effectiveness of any configuration in a specific direction of interest (θ_d, φ_d), the electric field magnitude at a desired point of interest (POI) can be expressed as

$$E_{\text{POI}} = \left| E(\theta_d, \varphi_d) \right|. \tag{5}$$

In our far-field model, regions are represented as directional cones (steradians). The HFP-based approach—recognized for accuracy and computational efficiency in modeling RIS-induced electromagnetic behaviors [2], [12]—enables detailed analysis of signal suppression and enhancement across specific angular domains for various RIS designs and frequency bands. This method scales effectively to multipath and NLoS scenarios, particularly when RIS units and transmitters/receivers are separated by large distances (exceeding 10λ) or when combined with ray-optics techniques [13].

III. SHIELD: A Novel Algorithm for RF-Fencing

To operationalize RF-Fencing in PWEs, we propose the SHIELD algorithm, a novel, codebook-driven approach leveraging physical modeling to enhance network covertness and mitigate jamming. SHIELD shapes signals in the angular domain by generating RIS $\mathbf{\Phi}$ to suppress EM radiation in undesired directions while maintaining signal quality within intended coverage zones. Its workflow-outlined in Alg. 1-requires only the identification of the SDAs and SSAs and the retrieval of corresponding beam-steering entries from the manufacturing phase thus avoiding computationally intensive iterative optimization and complete channel estimation during runtime. This design makes SHIELD suitable for real-world deployment even in dense, dynamically changing networks.

To quantify the SHIELD's performance for a total of k SDAs and SSAs, we utilize P_k which is given as

$$P_k = 20 \log_{10} \left(\frac{E_k^{\text{POI,final}}}{E_k^{\text{POI,initial}}} \right), \tag{6}$$

where $E_k^{\text{POI,final}}$ and $E_k^{\text{POI,initial}}$ denote the electric field magnitudes at the POI after applying SHIELD and under the initial, optimal beam-steering configuration, respectively. In the case of SDAs, values of P_k approaching 0 dB indicate that users experience nearly identical performance compared to conventional beam steering, thus preserving communication quality. Conversely, for SSAs, the objective is to maximize suppression, leading to strongly negative values of P_k that reflect effective mitigation of unintended emissions. In scenarios involving multiple SDAs or SSAs, the overall performance is obtained by computing the individual amplitude ratios for each region using Eq. (6) and averaging the resulting field values across all corresponding POIs.

Algorithm 1 RF-Fencing Algorithm for Signal Suppression and Signal Delivery Areas Creation Within the Network (SHIELD)

1: **Input:**
- Codebook Database with E_k for supported *AoA*/*AoD*.
- Number of d, u for SDAs and SSAs.
- Tolerance and learning rate μ and weight parameter w_{opt}.
- Thresholds τ_{SDA}, τ_{SSA}.
- Compromise factor η.

2: **Dominant Field Identification:** For each case k, identify dominant field values.

3: Form the masks for SDA and SSA, $\mathcal{M}_d$ and $\mathcal{M}_u$, respectively using Eq. (7).

4: **Common Field Computation:** Compute $\mathbf{E}_{\text{common}}$ as in Eq. (8) and obtain the initial $\mathbf{\Phi}_{\text{init}}$ from Eq. (9).

5: **Online Optimization:**
- Set $\mathbf{\Phi}_{\text{init}} \leftarrow \mathbf{\Phi}_{\text{common}}$.
- Define the cost function by evaluating Eqs. (10), (11).
- Update the $\mathbf{\Phi}$ using a gradient descent step according to Eq. (12):

$$\mathbf{\Phi}_{\text{opt}} = \mathbf{\Phi}_{\text{init}} - \mu \nabla_{\mathbf{\Phi}} \mathcal{J}(\mathbf{\Phi}).$$

6: **Output:** Final common phase profile $\mathbf{\Phi}_{\text{opt}}$ and performance metrics for SDAs and SSAs (Eq. (6)).

The first stage of SHIELD involves identifying the angular regions corresponding to SDAs and SSAs using precomputed E_{field} responses retrieved from the RIS codebook. Specifically, the algorithm takes as input the desired number of SDAs and SSAs, denoted by d and u, respectively. For each of these target directions, the corresponding field distribution $|E_{field}|$ is examined over the angular domain to identify dominant scattering components. Regions in which the field magnitude exceeds a threshold τ_{SDA} for SDAs or τ_{SSA} for SSAs are aggregated into direction-specific masks:

$$\mathcal{M}_d = \bigcup_{k=1}^{d} \{\, \theta, \varphi \;:\; |E_k| > \tau_{\text{SDA}} \, \max |E_d(\theta, \varphi)| \}$$
$$\mathcal{M}_u = \bigcup_{k=d+1}^{d+u} \{\, \theta, \varphi \;:\; |E_k| > \tau_{\text{SSA}} \, \max |E_d(\theta, \varphi)| \} \tag{7}$$

Based on the constructed masks, SHIELD synthesizes a composite EM response $\mathbf{E}_{\text{common}}$ that reflects the dominant SDA fields while mitigating emissions in undesired angular sectors. In particular, SHIELD computes the maximum of the SDA field components in areas where there is no overlap with the SSAs, while in overlapping regions, it applies a compromise factor η to balance the conflicting objectives of suppression and service preservation. Outside these designated regions, the field components are deliberately nulled to minimize unintended radiation. Thus, the composite field can be expressed as

$$\mathbf{E}_{\text{common}} = \begin{cases} \max\limits_{1 \le k \le d} E_k & \text{in } \mathcal{M}_d \setminus \mathcal{M}_u, \\ \eta \max\limits_{1 \le k \le d} E_k & \text{in } \mathcal{M}_d \cap \mathcal{M}_u, \\ 0 & \text{otherwise}, \end{cases} \tag{8}$$

Following this, the initial phase configuration for all RIS elements, denoted by $\mathbf{\Phi}_{\text{common}}$, is extracted from the argument of the composite field, as given by

$$\mathbf{\Phi}_{\text{common}} = \arg(\mathbf{E}_{\text{common}}), \tag{9}$$

where the operation $\arg(\cdot)$ returns the phase angle of the complex field values. This step provides an efficient near-optimal estimation of the $\mathbf{\Phi}_{\text{common}}$, similar to methods used in smart antenna arrays and analog beamforming for both far-field and near-field cases [14]. Consequently, a lightweight gradient-based procedure is used in order to fine-tune the initial guess of $\mathbf{\Phi}_{\text{common}}$ and correct minor deviations. By this approach, SHIELD workflow remains applicable for real-time RIS control offering the minimal computational overhead.

The upcoming optimization procedure is guided by a cost function that captures the discrepancy between the synthesized field and a set of target amplitudes in the angular masks $\mathcal{M}_d$ and $\mathcal{M}_u$, corresponding to the SDAs and SSAs, respectively. For each region type, the directional mismatch is computed as

$$\mathcal{J}_{d/u}(\mathbf{\Phi}) = \sum_{(\theta,\varphi) \in \mathcal{M}_{d/u}} \left| E(\mathbf{\Phi}; \theta, \varphi) - E_{\text{POI},d/u} \right|^2, \tag{10}$$

where $E(\mathbf{\Phi}; \theta, \varphi)$ represents the EM field (E_{field}) evaluated using the current configuration $\mathbf{\Phi}$, and $E_{\text{POI},d/u}$ denote the reference amplitudes within the SDAs and SSAs. These partial costs are then combined into a single objective function,

$$\mathcal{J}(\mathbf{\Phi}) = \mathcal{J}_d(\mathbf{\Phi}) - w_{\text{opt}} \, \mathcal{J}_u(\mathbf{\Phi}), \tag{11}$$

where the weight parameter w_{opt} balances the emphasis placed on suppressing signal leakage in the SSAs versus maintaining signal strength in the SDAs. Optimization is performed using a single-step gradient descent update given by

$$\mathbf{\Phi}_{\text{opt}} = \mathbf{\Phi}_{\text{init}} - \mu \nabla_{\mathbf{\Phi}} \mathcal{J}(\mathbf{\Phi}), \tag{12}$$

where μ denotes the learning rate (in m^2/V^2), and the initialization $\mathbf{\Phi}_{\text{init}}$ is set equal to $\mathbf{\Phi}_{\text{common}}$. The final configuration $\mathbf{\Phi}_{\text{opt}}$ is applied across the RIS elements to enforce the spatial signal shaping required by the RF-Fencing service.

Finally, the computational complexity of SHIELD is determined by the RIS size $N_{\text{el}} = N_r \times N_c$ and the number of iterations N_I required for convergence. Both dominant region identification and multiplexed field computation scale linearly with the number of RIS elements, i.e., $\mathcal{O}(N_{\text{el}})$, while the gradient-based refinement step requires full-array updates at each iteration, resulting in an overall complexity of $\mathcal{O}(N_I \cdot N_{\text{el}})$.

IV. Performance Evaluation

In this section, the performance of SHIELD in slicing the PWE into SDAs and SSAs is evaluated under various deployment scenarios involving both mmWave and THz frequency bands, as well as different RIS array dimensions. For all cases, the incident plane wave is defined with magnitude $E_0 = 1\,\text{V/m}$, which serves as a reference to evaluate the behavior of the scattered field. The resulting field in each observation direction is computed using the HPF as described in Sec. II, where the total scattered response arises from the coherent superposition of spherical wavefronts emitted by individual RIS elements. When these contributions align constructively, the overall field magnitude may exceed that of the original incident wave, revealing the spatial coherence effects induced by the RIS configuration.

A. THz Communication Network

The performance of SHIELD is first evaluated within a THz-band communication network, operating at a carrier frequency of 1 THz. The RIS is configured as a 50×50 element array, with an inter-element spacing of $\lambda_w/5$. To model the EM behavior of the system, the far-field expressions are employed, computing the scattered field E_{field} over an angular resolution of 1° to ensure precise evaluation of spatial field variations. During the manufacturing phase, a total of 500 precomputed, optimal beam-steering configurations, covering combinations of (AoA, AoD), are stored within the codebook for use during operation. The online evaluation focuses on the creation of two SDAs and one SSA. After a fine-tuning procedure, the input parameters for SHIELD include a convergence tolerance of 10^{-3}, an optimization weight factor of $w_{\text{opt}} = 0.5$, a learning rate of $\mu = 0.02$, and a compromise factor $\eta = 0.75$. Finally, the thresholds for identifying dominant regions are set to $\tau_{\text{SDA}} = 0.95$ and $\tau_{\text{SSA}} = 0.96$, respectively.

Fig. 2 illustrates SHIELD's performance, showing the E_{field} before and after SHIELD's application. Initially, SDAs at angles $(30^\circ, 75^\circ)$ and $(15^\circ, 165^\circ)$ exhibit field magnitudes of 1530.9 V/m and 2332.5 V/m, respectively, while the SSA at

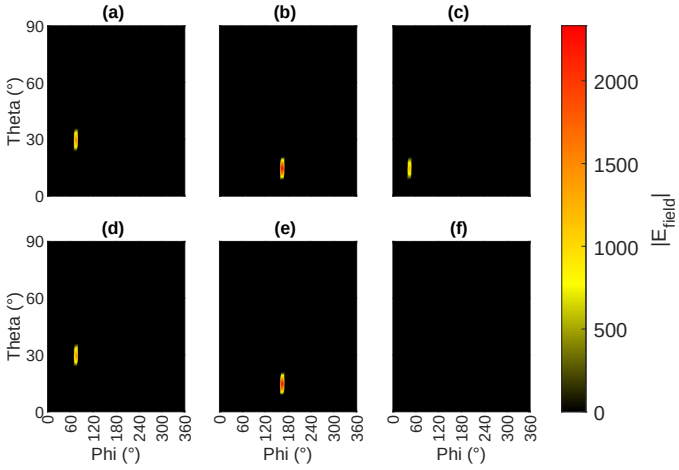

Fig. 2: E_{field} magnitude before (top) and after (bottom) SHIELD usage for SDAs (30°, 75°), (15°, 165°) and SSA (15°, 45°).

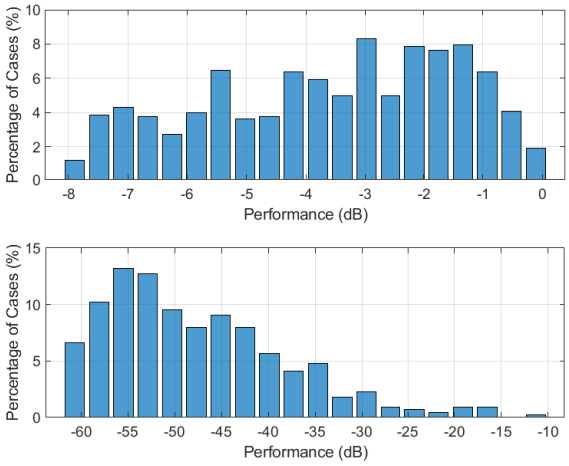

Fig. 3: Cumulative performance results across multiple cases for SDAs (up) and SSAs (down).

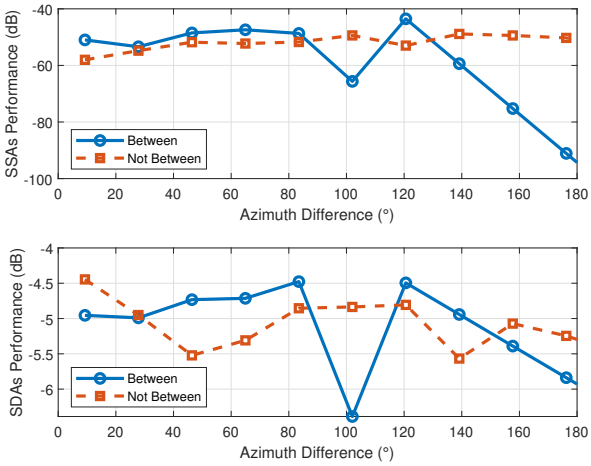

Fig. 4: Azimuthal difference effect when the single SSA lies between (blue) or outside (red) the two SDAs.

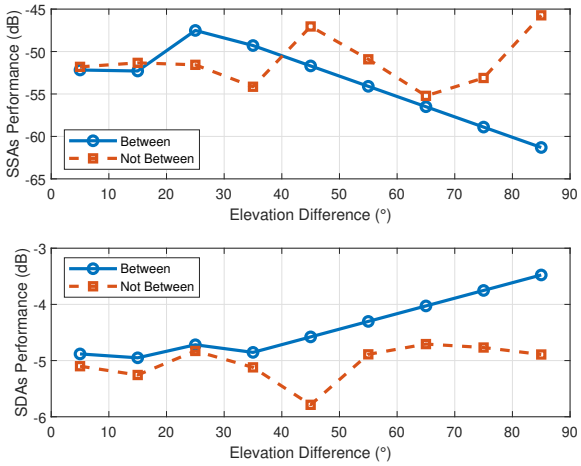

Fig. 5: Elevation difference impact on SHIELD performance for the same SSA/SDA layout categories as in Fig. 4.

$(15°, 45°)$ measures 1207.4 V/m. Post-SHIELD implementation, the SSA field strength significantly reduces to 0.41 V/m, leading to mitigation about -69.25 dB, with minimal SDA losses of only -0.49 dB and -0.24 dB, corresponding to magnitudes of 1447 V/m and 2269.4 V/m. These outcomes confirm SHIELD's efficacy in suppressing undesired directions while preserving intended communication channels.

Fig. 3 provides cumulative SHIELD performance data across 500 scenarios, highlighting both suppression efficacy and service continuity. For SSAs, suppression exceeds -50 dB in approximately 49.1% of cases, remains between -50 dB and -20 dB in 49.32%, and is below -20 dB in just 1.59%. Regarding SDAs, near-optimal performance (below 2 dB degradation) occurs in 29.3% of cases, moderate degradation within $[-4, -2]$ dB and $[-6, -8]$ dB occurs in 30.7% and 23.9%, respectively, and significant drops of up to -8 dB occur in only 16.1% of scenarios. These findings underline SHIELD's robustness in managing complex spatial suppression requirements alongside service continuity.

Figs. 4 and 5 explore SHIELD's sensitivity to angular separations between SDAs and SSAs. Fig. 4 reveals that when an SSA lies outside the SDA angular span, SHIELD achieves consistent suppression levels of approximately -50 to -60 dB. Even in challenging arrangements with the SSA between SDAs, suppression effectiveness remains robust, improving significantly as angular separation widens. Similarly, Fig. 5 shows suppression consistently around -45 to -65 dB for SSA, with SDA performance approaching optimal values as elevation differences increase.

B. mmWave Communication Network

In the second evaluation scenario at 300 GHz, the RIS configuration expands to a 75×75 array. Again, 500 precomputed beam-steering configurations accommodate broader mmWave beam characteristics. This scenario involves two SSAs and one SDA, setting more demanding suppression conditions.

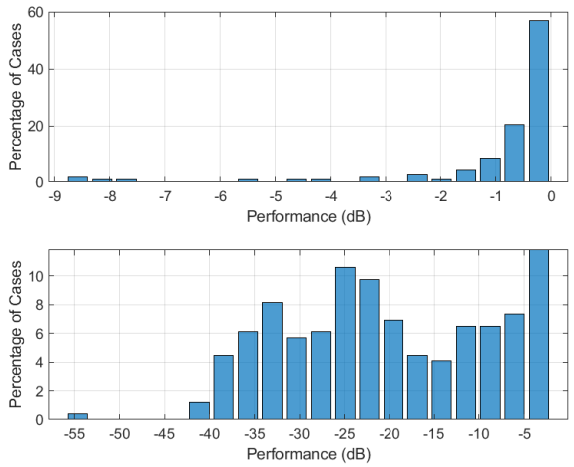

Fig. 6: Cumulative performance results across multiple cases for SDAs (up) and SSAs (down).

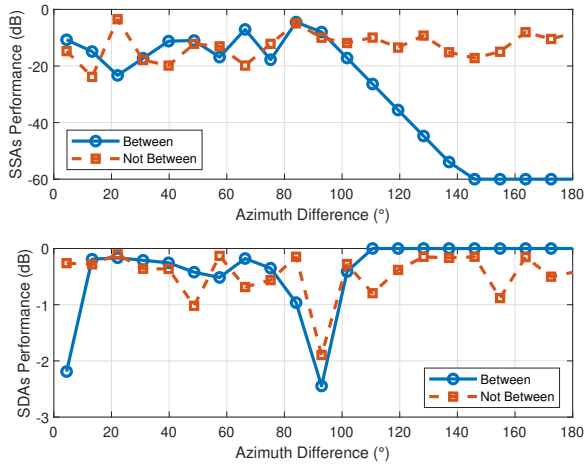

Fig. 7: Azimuth difference when SDA is between (blue) and not between (red) the SSAs.

After fine-tuning, parameters are established as thresholds $\tau_{\text{SDA}} = 0.97$, $\tau_{\text{SSA}} = 0.99$, compromise factor $\eta = 0.1$, optimization weight $w_{\text{opt}} = 150$, and learning rate $\mu = 0.02$.

Fig. 6 illustrates SHIELD's cumulative performance for the mmWave cases. SSA suppression exceeds -30 dB in 25% of scenarios, ranges between -30 dB and -10 dB in 50%, and remains significant in most remaining cases. Regarding SDA performance, 89.43% show negligible degradation compared to optimal beam-steering, with minor reductions ($[-4, -2]$ dB and $[-6, -4]$ dB) in only 4.8% and 2.4% of cases, respectively. Only 0.81% of scenarios experience reductions exceeding -8 dB, highlighting the inherent trade-offs in simultaneous multiple SSA management. Finally, Fig. 7 examines azimuthal separations, revealing minimal SDA impact and consistent suppression (-10 to -20 dB) when the SDA lies outside SSAs. When positioned between SSAs, suppression significantly improves with increasing angular separation, reaching up to -60 dB, while maintaining near-optimal SDA performance. These results confirm SHIELD's effective interference management and coverage precision in complex mmWave deployments.

V. Conclusion

This work introduced SHIELD, a novel codebook-based algorithm that enables spatially-aware covert communication within PWEs. Specifically, SHIELD dynamically configures multiple RISes to enforce electromagnetic suppression in targeted directions while maintaining high signal integrity in service areas. Extensive evaluations across THz and mmWave bands demonstrated SHIELD's ability to sustain strong suppression performance even in challenging configurations, including closely spaced SSAs and SDAs. Overall, SHIELD provides a scalable and efficient methodology for integrating directional privacy into next-generation wireless systems.

Acknowledgment

This work has received funding from the SNS-JU under the European Union's Horizon Europe research and innovation programme, in the frame of the NATWORK project (No 101139285) and CYBERSECDOME (No 101120779). The methodology was developed within CYBERSECDOME while NATWORK contributed to the experiments, key results, and conclusions.

References

[1] X. Chen *et al.*, "Covert communications: A comprehensive survey," *IEEE Commun. Surv. & Tut.*, vol. 25, no. 2, pp. 1173–1198, 2023.

[2] A. I. Papadopoulos *et al.*, "Physics-informed metaheuristics for fast RIS codebook compilation," *IEEE Communications Magazine*, 2024.

[3] A. Papadopoulos *et al.*, "An open platform for simulating the physical layer of 6g communication systems with multiple intelligent surfaces," in *2022 18th International Conference on Network and Service Management (CNSM)*, pp. 359–363, IEEE, 2022.

[4] S. I. Raptis and et al., "An accurate semi-analytical model for periodic tunable metasurfaces electromagnetic response," in *2024 18th European Conference on Antennas and Propagation (EuCAP)*, pp. 1–5, 2024.

[5] X. Lu *et al.*, "Intelligent reflecting surface enabled covert communications in wireless networks," *IEEE Network*, vol. 34, no. 5, pp. 148–155, 2020.

[6] S. Pejoski *et al.*, "Full-duplex covert communications assisted by intelligent reflective surfaces," vol. 26, no. 12, pp. 2846–2850, 2022.

[7] Y. Gao *et al.*, "Multi-RIS aided covert communications: A multi-agent reinforcement learning approach," *IEEE Trans. Cogn. Commun. Netw.*, 2024. Early Access.

[8] A. Papadopoulos *et al.*, "RIS as a network resource: User multiplexing and pricing algorithms," in *2024 3rd International Conference on 6G Networking (6GNet)*, pp. 144–152, 2024.

[9] A. Papadopoulos *et al.*, "On modeling the ris as a resource: Multi-user allocation and efficiency-proportional pricing," *IEEE Transactions on Network and Service Management*, pp. 1–1, 2025.

[10] C. Liaskos *et al.*, "Software-defined reconfigurable intelligent surfaces: From theory to end-to-end implementation," *Proceedings of the IEEE*, vol. 110, no. 9, pp. 1466–1493, 2022.

[11] M. Segata *et al.*, "CoopeRIS: A framework for the simulation of reconfigurable intelligent surfaces in cooperative driving environments," *Computer Networks*, vol. 248, p. 110443, 2024.

[12] A. Pitilakis *et al.*, "On the mobility effect in UAV-mounted absorbing metasurfaces: A theoretical and experimental study," *IEEE Access*, vol. 11, pp. 79777–79792, 2023.

[13] A. Pitilakis *et al.*, "Reconfigurable metasurface architecture for complete wavefront control in mmwave programmable wireless environments," in *2023 Seventeenth International Congress on Artificial Materials for Novel Wave Phenomena (Metamaterials)*, pp. X–267–X–269, 2023.

[14] C. A. Balanis, *Antenna Theory: Analysis and Design*. John Wiley & Sons, 2016.